# 14

# *Biogeochemical Variability at the Sea Surface: How It Is Linked to Process Response Times*

**Amala Mahadevan and Janet W. Campbell**

**CONTENTS**

## 14.1 Introduction

The sea surface distributions of many biogeochemical tracers are highly correlated in space and time on meso (10 to 100 km) and smaller scales, but their scales of variability differ. Some tracers like sea surface chlorophyll (Chl) are patchier or finer scaled than others, such as sea surface temperature (SST) (Figure 14.1). This work aims to characterize the spatial distributions of various tracers in terms of a variance-based measure of their patchiness. Using a scaling argument and a numerical model, we relate the patchiness of a tracer distribution to the characteristic response time $\tau$ of the tracer to processes that alter its concentration in the upper ocean. This enables us to relate the distributions of different tracers in the upper ocean and provide an estimate for the relative size of the grid spacing needed to observe or model different tracers. We also suggest a scaling relationship to infer the mean rate of upwelling in a region from the mean vertical concentration profile of a tracer and *a priori* knowledge of the characteristic response time $\tau$ of the tracer.

## 14.2 Tracer Distributions and Transport

Many biogeochemical tracers in the ocean, like dissolved inorganic carbon (DIC), oxygen, nitrate, phosphate, dissolved organic nitrogen and carbon (DON and DOC), as well as physical variables like temperature and salinity, change rapidly with depth in the upper 500 or so meters of the ocean (Figure 14.2). Tracer

0-8493-1344-9/04/$0.00+$1.50

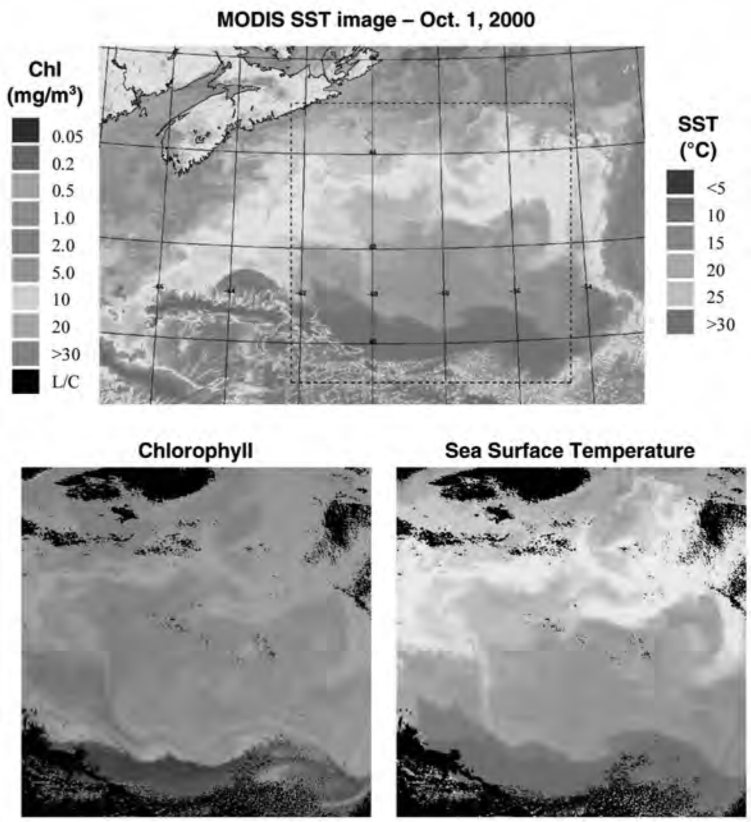

**FIGURE 14.1 (Color figure follows p. 332.)** Simultaneous satellite images of Chl (lower left) and SST (upper center and lower right) in the western Atlantic Ocean south of Nova Scotia acquired by the Moderate-resolution Imaging Spectroradiometer (MODIS) on October 1, 2000. The region shown in the two lower panels is indicated by a dotted outline in the upper panel and is approximately 512 × 512 km$^2$. The resolution of the data is approximately 1 × 1 km$^2$. The color scale is logarithmic for Chl, but linear for SST. Black areas in the two lower panels are clouds.

concentration gradients in the thermocline are orders of magnitude larger in the vertical than in the horizontal. This is largely because these tracers are modified in the upper ocean by various processes (such as phytoplankton production, air–sea gas exchange, heat fluxes, and evaporation–precipitation), but rates of vertical exchange that convey these changes to the interior are extremely small. The mean vertical tracer concentration profiles result from a balance between the rate at which the tracer is modified by nonconservative processes that act primarily in the upper ocean, and the rate at which it is transported or mixed vertically. A small rate of vertical exchange (as compared to rate of modification) results in a steep profile, while a higher rate results in a more homogeneous vertical distribution.

Vertical transport across the thermocline is vital to the exchange of properties between the atmospherically forced surface ocean and its interior. Within the thermocline, rates of small-scale diapycnal mixing are far too weak to account for the observed rates of exchange of properties. Vertical transport is thought to occur on meso- and smaller-scales largely via the advection associated with the strain and divergence of the horizontal flow field. Sloping isopyncal surfaces, which may be termed fronts, act as pathways for vertical motion (Figure 14.3). Thus, vertical velocities are pronounced at fronts (Pollard and Regier, 1992; Voorhis and Bruce, 1982), or along the edges of meanders and eddies (Levy et al., 2001). Upwelling velocities can be of the order of tens of meters per day, but away from boundaries and topography, it is generally episodic and occurs on scales smaller than the internal Rossby radius of deformation that are associated with the sub-mesoscale dynamics (1 to 10 km in the horizontal). Convective and shear-induced mixing facilitates communication between the upper thermocline, lower mixed layer, and the surface ocean, exposing to the surface substances transported isopycnally up to the mixed-layer base.

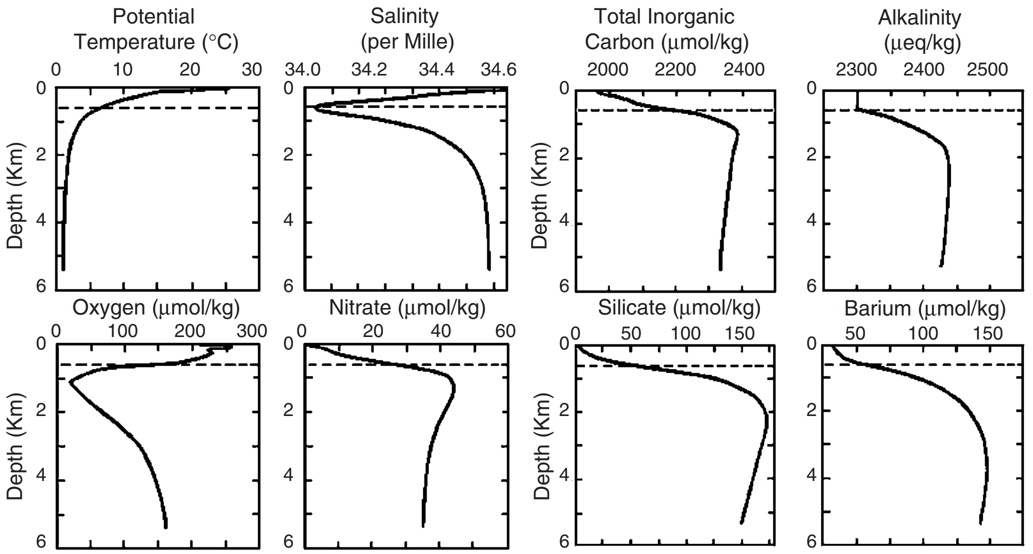

**FIGURE 14.2** Typical vertical profiles from the Pacific Ocean showing strong concentration gradients in the thermocline. (Reproduced from GEOSECS data displayed on the Web.)

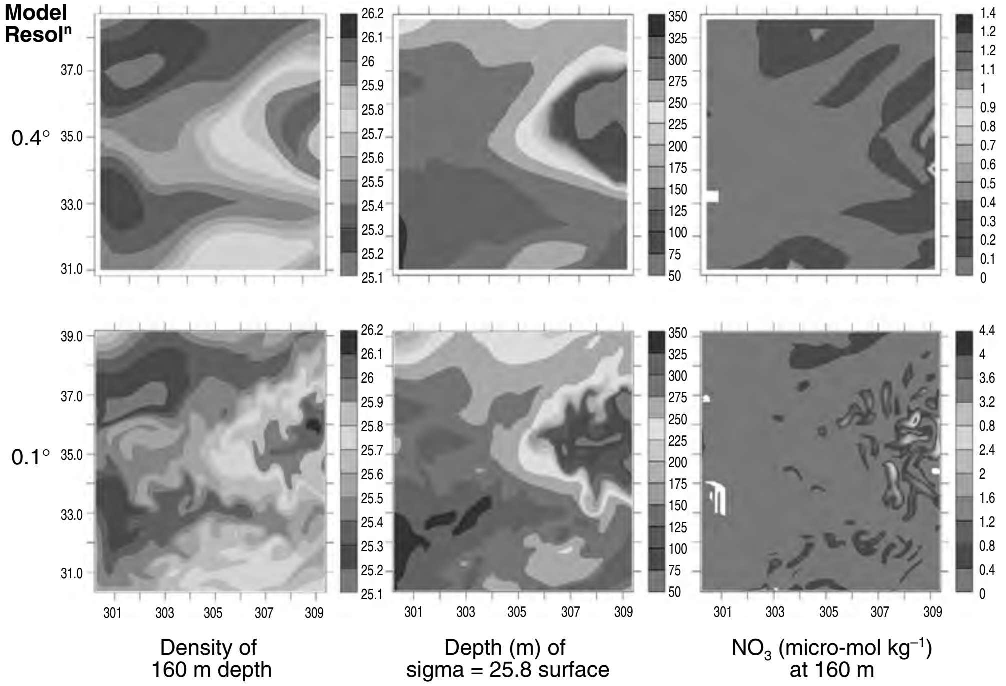

**FIGURE 14.3 (Color figure follows p. 332.)** Model potential density and nitrate fields from a 10° × 10° region representative of the oligotrophic subtropics near Bermuda depict that nitrate is fluxed into the euphotic zone where isopycnals outcrop. The fields are shown at two different model resolutions to demonstrate the importance of resolving the small scales (less than the internal Rossby radius) in capturing vertical advective transport. The dimensions of the domain are in degrees latitude and longitude.

Because the tracer concentration gradients are typically very large in the vertical, the upwelling of water from the thermocline to the mixed layer introduces a different concentration at the surface. Therefore, in many regions of the pelagic ocean, variations in the surface distribution of tracers are induced largely by upwelling. While upwelling introduces tracer anomalies in the surface, upper ocean processes typically tend to annihilate the anomalies and restore the concentration to its background surface value. In the oligotrophic ocean, for example, phytoplankton nutrients such as nitrate and phosphate are depleted in the surface ocean. Frontal upwelling brings nutrients to the surface layer at certain places, simultaneously introducing an anomalous signature in temperature, DIC, $O_2$, etc. The increased nutrient supply results in new production of phytoplankton, reflected in increased Chl values. As the upwelled nutrients are consumed, the surface is restored to its oligotrophic state. Biological production also consumes DIC and liberates $O_2$, tending to annihilate the DIC and $O_2$ signals introduced by upwelling. In addition, air–sea gas exchange tends to equilibrate the surface concentrations of dissolved $O_2$ and $CO_2$ with the atmosphere. The timescale of equilibration depends on the wind speed and surface conditions (affecting the so-called piston velocity) and the mixed-layer depth. Although gas exchange equilibrates the mixed layer $O_2$ with the atmosphere typically in a month's time, DIC takes almost a year to attain equilibrium because of the reactions buffering $CO_2$ in seawater. The remineralization of sinking organic matter at depth maintains the large-scale vertical gradients, but it is mainly upwelling and the upper ocean processes that affect the surface distribution characteristics of the various biogeochemical substances. Surface anomalies are consequently advected at the surface and bear the signature of stirring by surface eddies and currents (Figure 14.1).

As many biogeochemical tracers possess a strong vertical concentration gradient, are affected by the same physical dynamics and often even the same upper-ocean nonconservative processes, it is no surprise that their sea surface distributions are highly correlated, particularly on spatial scales of 10 to 100 km and temporal scales of weeks. It thus seems plausible that by relating various tracers and processes, one might be able to diagnose the distribution of a biogeochemical tracer such as DIC or $O_2$ from remotely sensed variables like SST and Chl. This work takes a first step in this direction. We begin by analyzing various tracer distributions and finding a diagnostic by which to differentiate them. We then explain the observed differences in their distributions.

A significant and quantifiable difference among various tracers is their spatial heterogeneity. Variables like Chl are finer scaled or patchier than others, such as SST. In model simulations, we find that the variability of $O_2$ is finer scaled than that of DIC. We believe that such differences arise primarily because of the varied response of the tracers to processes that alter their concentration at the surface. In the pelagic ocean, upwelling occurs on fine scales (~1 km). In the meso- and submeso-scale range (1 to 100 km), tracers that are modified or restored rapidly at the surface tend to be finer scaled or patchier than those that equilibrate slowly. In this work, we analyze tracer distributions in terms of variance and suggest a variance-based measure of patchiness. We characterize the tracer's response to nonconservative upper ocean processes in terms of a characteristic (e-folding) response time $\tau$, and show how the patchiness of the distribution of the tracer in the upper ocean varies with $\tau$ (Mahadevan and Campbell, 2002).

## 14.3 Quantifying Variability

We use a variance-based empirical approach to characterize the spatial heterogeneity of a tracer at the sea surface and demonstrate the technique using data from remote sensing and model simulations. In contrast to methods such as spectral analysis (Denman and Platt, 1975; Gower et al., 1980), semivariogram analysis (Yoder et al., 1987, 1993; Glover et al., 2000; Deschamps et al., 1981) and autocorrelation analysis (Campbell and Esaias, 1985), this method does not invoke the assumption of isotropy in the two-dimensional spatial distributions. We calculate the variance associated with a characteristic length scale $L$, as the average variance contained within regions of area $L^2$. Beginning with the largest scale $L_1$, which is the size of the whole domain, we first compute the total variance within this domain, $V_1$. Next, we partition the domain into four quadrants, and calculate the average variance $V_2$, associated with length scale $L_1/2$. We continue to partition each subdomain into quadrants with successively smaller dimensions: $L_1/4$, $L_1/8$, … and compute the average variance at each scale. The average variance within

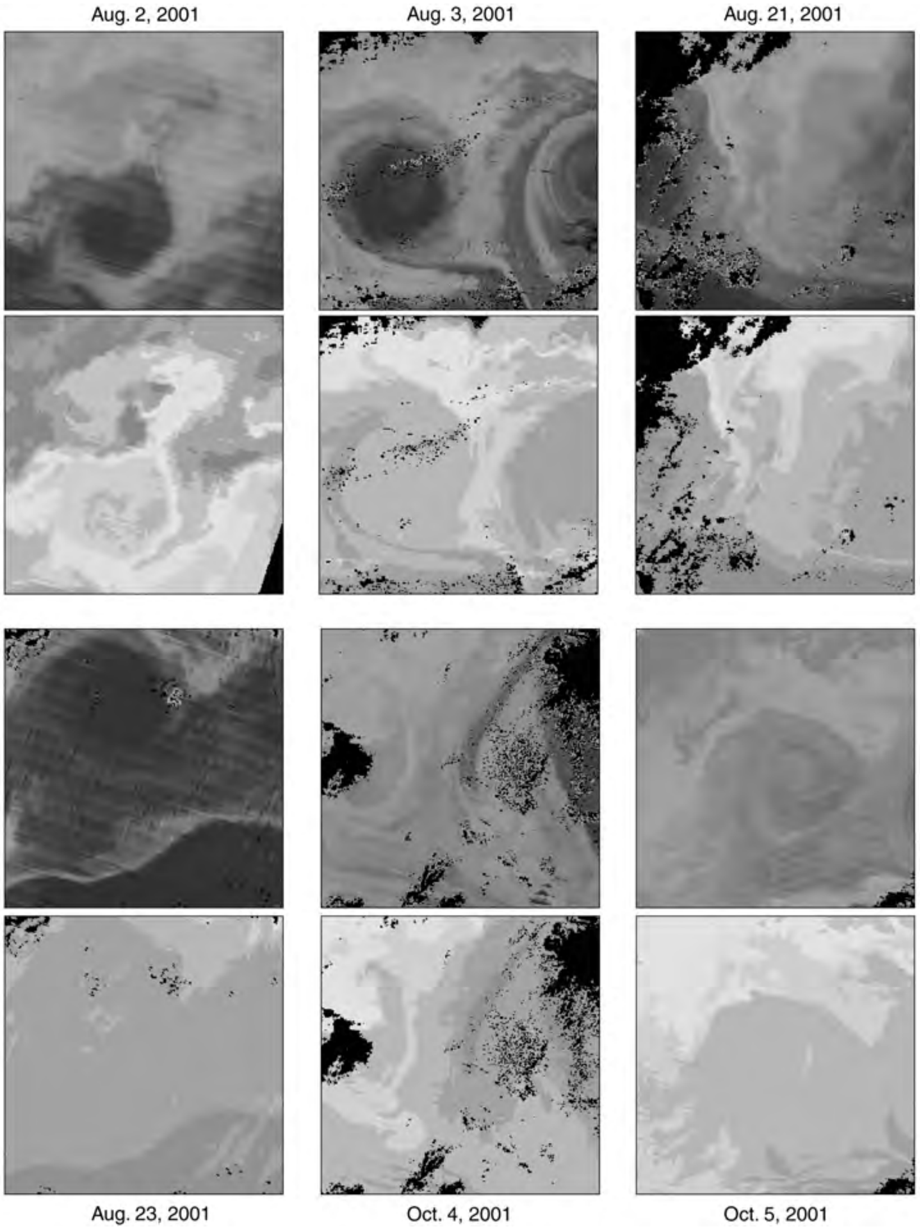

**FIGURE 14.4** **(Color figure follows p. 332.)** Simultaneous satellite images of chlorophyll (Chl) and sea-surface temperature (SST) for domains of size 256 × 256 km$^2$ and resolution 1 × 1 km$^2$ in the western Atlantic continental shelf and slope region acquired by MODIS on six dates between August 2 and October 5, 2001. In each case, the Chl image is above the SST image. Color scales are the same as those shown in Figure 14.1.

the length scale $L$, $V(L)$, can be normalized by the total variance within the domain $V_1$, to facilitate the comparison of different variables like SST and Chl.

This simple empirical technique relates to the more familiar method involving the variance (or power) spectrum. A variance spectrum *partitions* the total variance into components at wavenumbers $\nu = 1/L$, and is normally expressed as a power law function of the wavenumber. Our method expresses the average variance within areas of size $L^2$, and thus all variance at length scales *less than or equal to L*, or wavenumbers greater than or equal to $\nu$. Since the variance spectrum is the incremental change in variance $V$ for each wavenumber, it would be analogous to the derivative of $V$ with respect to $\nu$.

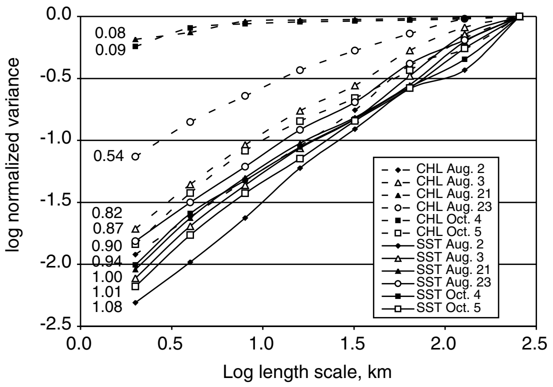

**FIGURE 14.5** Variance-scale (*V–L*) relationships in SST (solid lines) and Chl (dashed lines) for the MODIS satellite images shown in Figure 14.4. The slopes *p* are indicated to the left of each curve. The difference in the Chl and SST distributions can be diagnosed from the slopes of these lines. The shallower slope of the Chl (as compared to SST) curves indicates that Chl is patchier than SST.

### 14.3.1 Analysis of Satellite Data

We have applied this method to satellite-derived distributions of Chl and SST from the Moderate-resolution Imaging Spectroradiometer (MODIS) (Esaias et al., 1998), and to Chl from the Sea-Viewing Wide Field-of-view Sensor (SeaWiFS) (McClain et al., 1998) matched with SST from the Advanced Very High Resolution Radiometer (AVHRR) (McClain et al., 1985). The satellite data are approximately at $1 \times 1$ km$^2$ spatial resolution and are analyzed for areas approximately $256 \times 256$ km$^2$ in size. In the regions analyzed, upwelling that brings colder waters to the surface also brings nutrients that fuel biological production. Hence, high Chl is generally associated with lower temperatures. A sampling of the several SST and Chl views analyzed is shown in Figure 14.4. For both SST and Chl, the plot of $V(L)$ vs. $L$ on log–log axes (Figure 14.5) tends to be more or less linear, suggesting a power law relationship of the form:

$$V \sim L^p \tag{14.1}$$

where $p > 0$. Here we have normalized the variance by the total variance $V_1$, since we are more concerned with the exponent $p$, which reflects the degree of fine-scale structure or patchiness in the field.

If most of the variance in a tracer field exists at small scales, then the exponent $p$ will be relatively small. That is, $V(L)$ increases with $L$ much more rapidly at small $L$ than at large $L$, as compared to the case when the spatial variability is at large scales. In each of the cases analyzed, the slope of the variance curve for Chl is clearly smaller than that for SST, demonstrating that Chl is finer scaled or patchier than SST over this range of scales (2 to 256 km). When $p$ is constant over a range of scales, we infer that there is one dominant process operating over that range of scales. While the actual variance in a variable may vary by as much as two orders of magnitude from one time or place to another, the exponent $p$ varies much less. The exponent $p$ does not usually exceed 1, indicating that the increase in $V$ with $L$ slows with increasing $L$, i.e., the curvature of the $V(L)$ curve in linear space is negative.

The relationship between these $V$–$L$ curves and the variance spectrum is seen by taking the derivative of Equation 14.1 with respect to the wavenumber $\nu$, where $\nu = 1/L$, as follows:

$$dV/d\nu \sim d(\nu^{-p})\,/\,d\nu \sim -p\nu^{-p-1} \tag{14.2}$$

The $p$ exponents for Chl and SST in Figure 14.5 thus translate into variance spectrum exponents between –1.1 and –2.1, which are similar to values reported by others.

### 14.3.2 Analysis of Model Fields

We next apply this method to analyze model-generated surface fields of SST, new production, DIC, dissolved oxygen, and two idealized tracers that resemble $H_2O_2$ and DOC (Figure 14.6). The model is

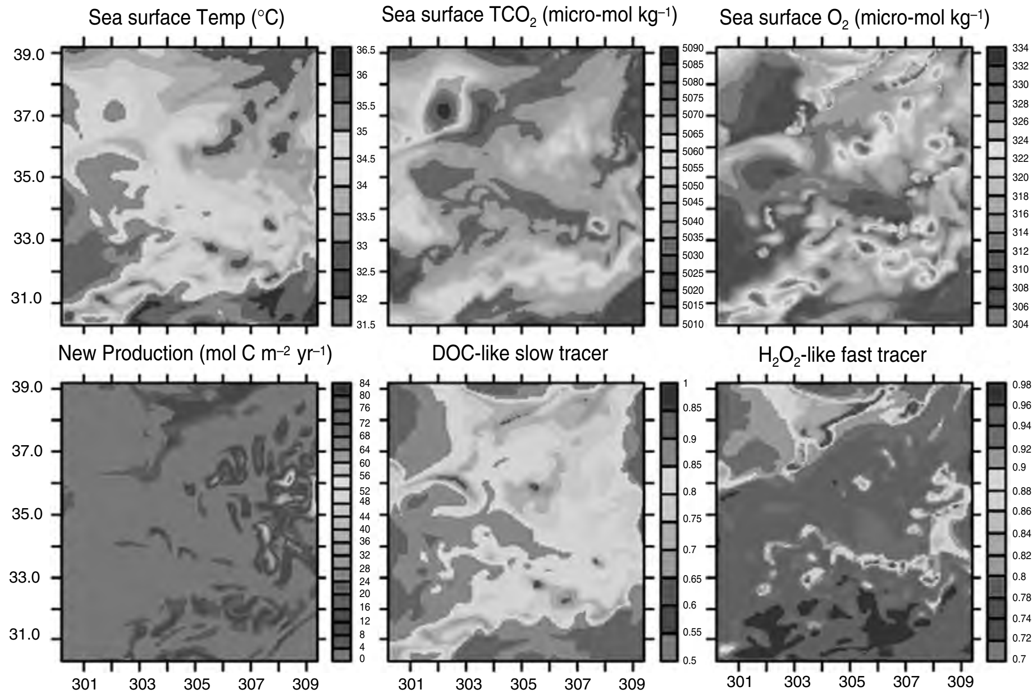

**FIGURE 14.6 (Color figure follows p. 332.)** Sea surface distribution of temperature, DIC, $O_2$, new production, DOC, and $H_2O_2$ from a limited region model of a 10° × 10° region in the subtropical Atlantic near Bermuda (Mahadevan and Archer, 2000). The model was driven at the open boundaries by dynamic fields from a global circulation model (Semtner and Chervin, 1992). The picture depicts a typical snapshot view of the ocean surface in the autumn, modeled at 0.1° resolution. The different tracers exhibit different scales of variability.

a fully three-dimensional nonhydrostatic model that is deployed at 0.1° resolution within a 10° × 10° region of the subtropical gyre near Bermuda (Mahadevan and Archer, 2000). It is forced at the open boundaries with time-dependent flow fields from the coarser resolution global circulation model of Semtner and Chervin (1992). The biogeochemical tracers in the model are initialized to resemble data from the Bermuda Atlantic Time Series site, and salinity and temperature are restored to monthly climatological values from Levitus (1982). The upwelling of nitrate fuels new production, which occurs within the euphotic layer with the uptake of the upwelled nitrate and DIC and the release of oxygen. The characteristic (e-folding) timescale for biological new production is taken to be 3 days. Oxygen and DIC are also altered by air–sea gas exchange that occurs with a constant piston velocity of 3 m per day. But $CO_2$ buffering slows the air–sea equilibration of DIC by a factor of 10 (the Revelle factor) as compared to $O_2$. Remineralization of the organic matter at depth restores the dissolved nitrate and carbon in the ocean, but the surface distributions of these tracers are clearly affected by the net biological production near the surface, rather than the remineralization at depth. The two idealized tracers that resemble $H_2O_2$ and DOC are initialized with an exponential profile that ranges from 1 at the surface to 0 at depth over an e-folding depth of 100 m. They are linearly restored to this steady-state profile, but one of these tracers ($H_2O_2$) is fast acting and has an e-folding time of 3 days, while the other (DOC) is restored with an e-folding time of 60 days. From viewing the surface model fields (Figure 14.6), it is evident that the distributions of new production, oxygen, and the fast-acting $H_2O_2$-like tracer are finer scaled than those of SST, DIC, and the slower-acting DOC.

Analysis of the surface fields with the variance method (Figure 14.7) confirms that the $H_2O_2$-like tracer, new production, and oxygen are patchier (have smaller *p*) than the DOC-like tracer, SST, and DIC. The patchier tracers are those that equilibrate more quickly at the surface, or respond more rapidly to processes that alter them. We therefore seek to characterize tracer patchiness in terms of the characteristic response time of the tracer to processes that alter it.

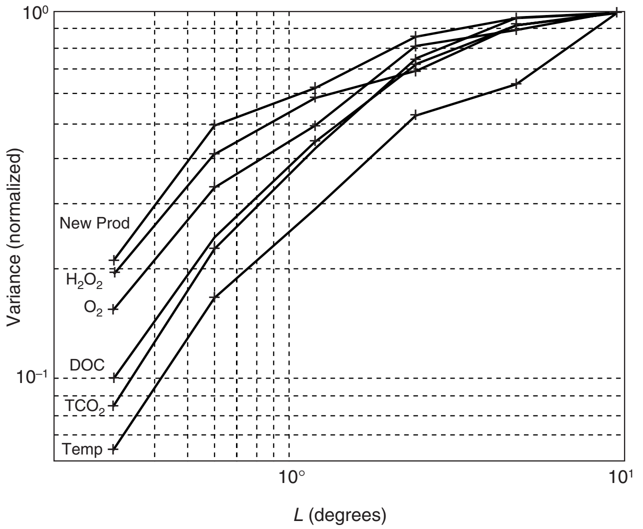

**FIGURE 14.7** Log–log plot of the average variance *V* vs. *L* for the model fields shown in Figure 14.6. The spatial heterogeneity of each tracer is characterized by its slope *p*; smaller *p* corresponds to greater patchiness.

## 14.4 Modeling and Results

### 14.4.1 How Patchiness Relates to Response Time τ

A simplified model for the distribution of a tracer, whose concentration is denoted by *c*, is given by

$$\frac{\partial c}{\partial t} + u_H \bullet \nabla_H c + w\partial_z c = S \tag{14.3}$$

where $u_H$ and $w$ denote the horizontal and vertical velocity of the fluid, $\nabla_H$ is the horizontal gradient operator, $\partial z$ is the vertical gradient operator, and *S* is a source or sink term to account for the modification of the tracer by nonconservative processes. *S* can often be written in terms of a characteristic timescale τ and concentration *c* as $S = -\tau^{-1}c$. In the case of a nutrient-like tracer depleted by biological uptake within the euphotic layer, τ is a characteristic e-folding timescale for biological production. Similarly, for air–sea gas flux modeled in terms of a wind speed–dependent piston velocity *k* and air–sea concentration gradient $\Delta c$, the characteristic time scale is $\tau = (\Delta z/k)(\Delta c/c)$, where $\Delta z$ is the mixed layer depth. Heat flux and evaporation–precipitation are often accounted for by restoring the temperature and salinity fields at the surface in a model to observed values with a characteristic restoration timescale τ. Thus for any process, one can identify a characteristic response time τ. Our aim is to characterize the distribution of the tracer as a function of τ.

We do this within the framework of a model. The above model (Equation 14.3) is used with $S = -\tau^{-1}c$ in the upper 95 m to represent the biological consumption of nutrient in the euphotic layer of the oligotrophic ocean. The nutrient-like tracer concentration *c* is initialized to resemble nitrate; it is abundant at depth, has a strong concentration gradient in the thermocline, and is depleted in the euphotic layer (taken to be the upper 95 m in the model), but is horizontally uniform at initialization. The tracer model is coupled to a three-dimensional dynamic model configured to simulate an upper ocean front. The model domain is a periodic channel 258 km in zonal extent and 285 km in meridional extent with solid north–south boundaries and periodic east–west boundaries. The grid spacing is approximately 4 km and 4.45 km in the zonal and meridional directions, respectively. In the vertical, we maintain the uppermost layer as 60 m, while the layers below vary in thickness from 16 m in the thermocline to 100 m at depth. The model domain is initialized with fresher water in the southern half of the channel to create an across-channel density front that is accompanied by an east–west geostrophic jet. As the model simulation progresses, the jet and front meander and set up a more complex flow that we assume to be representative of the ocean. Nutrient is upwelled into the euphotic zone (upper 95 m), where it is consumed at a rate $S = -\tau^{-1}c$ due to biological production. We use six different values of $\tau$, 2.5, 5, 10, 20, 40, and 80 days, in our numerical experiments to examine the relation between $\tau$ and the surface distribution of the tracer. The tracers are identically initialized and subject to the same dynamics; they vary only in their response times $\tau$.

If we assume a balance between the terms that represent the upwelling of nutrient into the euphotic layer and its uptake in Equation 14.1, we can write

$$\frac{W}{h}\left(c' - c_{\infty}\right) \sim -\frac{c'}{\tau} \tag{14.4}$$

where $c'$ and $c_{\infty}$ are the concentration of the tracer anomaly at the surface and the concentration at a depth $h$ below the mixed layer. Both $c'$ and $c_{\infty}$ are normalized by the mean surface concentration. Thus $(c' - c_{\infty})/h$ represents the vertical concentration gradient in the thermocline, and $W$ is the characteristic vertical velocity. Rearranging terms in Equation 14.4 gives

$$\left(1 - \frac{c_{\infty}}{c'}\right) \sim -\frac{1}{\bar{\tau}}$$

where $\bar{\tau} = \tau W / h$ is the ratio of the tracer response time to the vertical advection timescale. (Its inverse $h/(\tau W)$ is known as the Damköhler number.) Taking the logarithm of this relation gives

$$\log c' \sim \log c_{\infty} + \log \bar{\tau}. \tag{14.5}$$

The variance $V \sim c'^2$ and patchiness $p = \log V / \log L$. Therefore, by assuming that $p$ is constant over the range of length scales considered, we infer that

$$p \sim \log c_{\infty} + \log \bar{\tau}. \tag{14.6}$$

This suggests that when several tracers are subject to the same flow ($W/h$ is the same for the tracers), we can relate their spatial heterogeneity (measured by $p$) to their response time $\tau$. The index $p$ not only increases with $\tau$, but is more sensitive to $\tau$ when $\tau$ is relatively small.

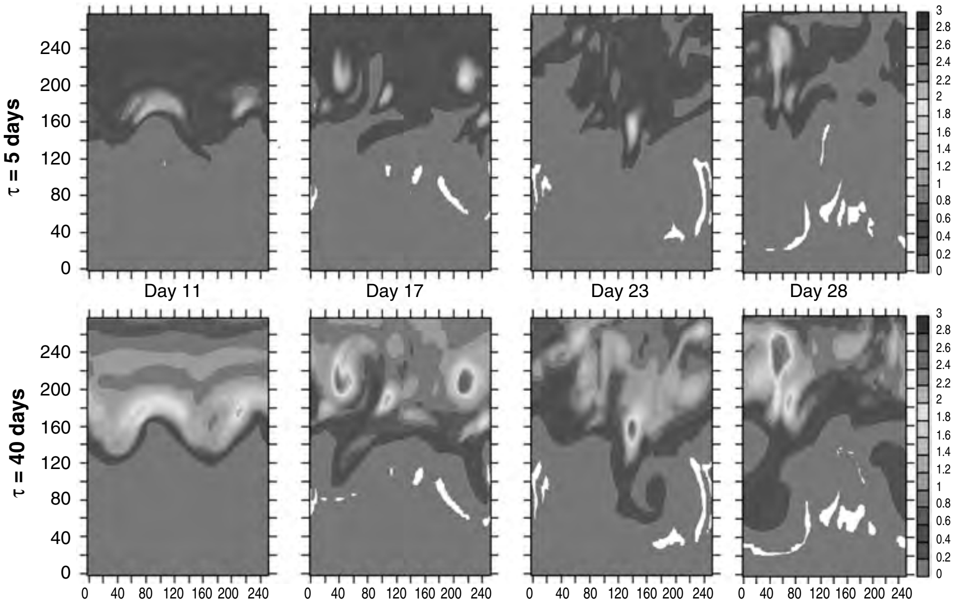

**FIGURE 14.8 (Color figure follows p. 332.)** Concurrent views of the surface concentration of the nutrient-like tracers with different response times $\tau$, averaged over the upper 95 m in the model. The tracer with smaller $\tau$ is patchier. The domain dimensions are in kilometers.

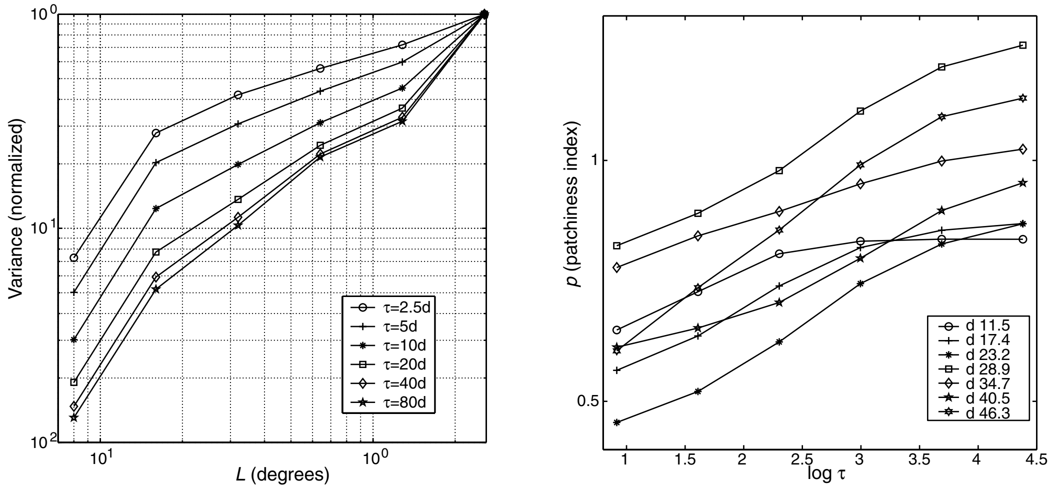

**FIGURE 14.9** (A) Log–log plots of the average variance *V* vs. *L* generated from concurrent snapshots of the tracers with different τ. The analysis demonstrates that tracers with small τ have shallower *V–L* curves or smaller values of *p*. (B) The slopes *p* of the *V–L* analysis plotted vs. log τ, at different times (days) in the simulation to verify the scaling relation (Equation 14.6).

*Model Results:* We now use results from the model described above to verify the scaling relation (Equation 14.6). In Figure 14.8 we show snapshots of the average tracer concentration in the upper 95 m of the ocean for the nutrient-like tracers that differ in their characteristic response times τ. The tracer with smallest τ is the patchiest; because the tracer at the surface is rapidly obliterated by biological consumption, only recently upwelled tracer is visible. As τ is increased, the tracer patches at the surface persist for longer and expand as they continue to be fed by upwelling from the subsurface while also being advected by the horizontal flow field. The variance analysis (curves of $V(L)$ in log–log space) for tracers with different τ in Figure 14.9A show a systematic increase in *p* (decrease in patchiness) with response time τ. We estimate the slope *p* of the curves in Figure 14.9A using their central portions and plot this patchiness measure *p* vs. log τ at different instances during the simulation (Figure 14.9B). The plots are linear and support the scaling relation 14.6. The deviation from linearity is most pronounced at early stages in the simulation for tracers with large τ that have not attained their full surface concentration.

## 14.4.2 Dependence of the Vertical Distribution of a Tracer on τ

The time-averaged concentration profiles of tracers, like those described here, are set largely by the balance between the rate of upwelling and their rate of alteration in the upper ocean. By averaging Equation 14.3 in the horizontal and assuming that over long times, the vertical concentration profiles of these tracers are in steady state, we find that the average concentration in the surface layer $\bar{c}$ varies as

$$\left(D/h^2\right)\left(\bar{c}-c_\infty\right) \sim -\bar{c}/\tau. \tag{14.7}$$

Here *D* represents an effective diffusivity that accounts for the averaged vertical transport, *h* represents a scale height over which the transport occurs, and $h^2/D$ is the *mean* upwelling timescale (different from the *local* upwelling timescale $h/W$). Rearranging Equation 14.7 gives

$$\bar{c}/c_\infty = \left(1+h^2/(D\tau)\right)^{-1} \tag{14.8}$$

a relation linking the mean vertical concentration profile characteristics of the tracer to the ratio of its characteristic response time and mean upwelling timescale. We can now use the results of the model to verify Equation 14.8. Because the variable parameter in the model is τ, we rewrite Equation 14.8 as $\tau^{-1} = (c_\infty/\bar{c}-1)D/h^2$ and plot $c_\infty D/\bar{c}h^2$ vs. $\tau^{-1}$ at different times in the model simulation (Figure 14.10). $D/h^2$ varies with time, but at each time in the simulation $c_\infty/\bar{c}$ scales with $\tau^{-1}$. The plots collapse into

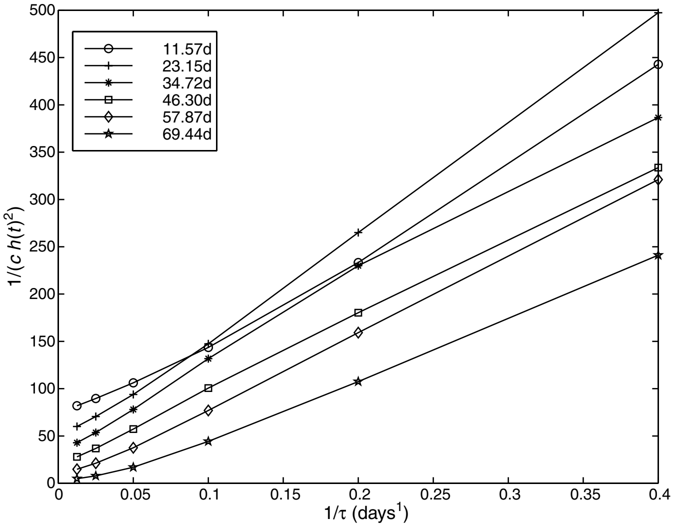

**FIGURE 14.10** The relation between the mean sea surface concentration of a tracer $\bar{c}$ and τ is tested by plotting $c_\infty D/\bar{c}h^2$ vs. $\tau^{-1}$ at different times in the simulation. $\bar{c}$ is taken to be the mean over the upper 95 m in the model. $D$ and $c_\infty$ are taken to be constant, and $h$ is assumed to increase linearly with time as this makes the plots collapse into a narrow region.

a narrow region if we take $h$ to increase linearly with time as the simulation progresses. The relation (Equation 14.8) implies that in regions where the time-averaged horizontal concentration gradients of a tracer are non-zero, we can use their vertical distributions to infer the mean rate of upwelling or effective diffusivity $D$ given a characteristic e-folding timescale τ with which the tracer is altered in the upper ocean.

### 14.4.3 Resolution Requirements for Tracers with Different τ

Tracers with short response timescales τ are finer scaled and patchier than those with large τ. Thus, they need to be sampled or modeled at higher resolution if the intention is to capture their variability. If, for example, we wish to capture a fixed proportion (say, 80%) of the variance in a region by sampling or modeling, an appropriate choice for the (nondimensional) horizontal grid size Δ is given by substituting $V = 0.8$ and $L = \Delta$ in Equation 14.1. Taking into consideration the negative sign generated by log(0.8), this implies that, $\log \Delta \sim -1/p$, which when combined with Equation 14.6 gives

$$\Delta \sim \exp(-1/(\log\bar{\tau} + \log c_\infty)). \tag{14.9}$$

Thus, two tracers that differ in their response times by a factor of 10 (and do not differ in their normalized depth concentrations $c_\infty$), differ in their model resolution requirement by a factor of 4. If biological production were negligible and air–sea exchange were the dominant process modifying DIC and $O_2$ at the sea surface, and if the normalized depth concentrations are assumed to be nearly the same, a factor of 10 difference in their equilibration times (1 month for $O_2$ vs. 10 months for DIC) would imply that $O_2$ requires four times higher resolution for observing or modeling than DIC. Similarly, Chl, which responds on a timescale of approximately 3 days, requires four times more resolution than SST, which responds to surface heat fluxes on a timescale of approximately 30 days. This explains why biological variables that are typically altered on short time scales are particularly difficult to observe and model in the ocean as compared to physical variables like temperature and salinity.

## 14.5 Discussion

The modification of tracers by nonconservative upper ocean processes can generally be parameterized in terms of a characteristic timescale τ and the tracer concentration $c$. Thus, even though the model used to derive the above results is simple, it can be generalized to various tracers and processes. When multiple processes modify a tracer, the effective characteristic timescale $\tau_{\mathrm{eff}}$, is the geometric mean of the individual process time scales $\tau$. Since patchiness of a tracer scales inversely as the index $p$, and $p \sim \log \tau$, tracer distributions are more sensitive to changes in $\tau$ when $\tau$ is small, but relatively insensitive when $\tau$ is large. In an ecosystem carbon cycle model, the variability in the DIC field is more sensitive to the choice of the biological time constants than to the piston velocity that determines the timescale of air–sea exchange, because the timescales of biological production are typically much smaller than those for air–sea exchange.

The relationships described here in terms of spatial distributions can be extended to the temporal context using intermittency as the analogue of patchiness. Further work needs to be done in verifying these ideas with oceanographic data. Since high spatial resolution *in situ* data are difficult to obtain, it may be more feasible to examine these ideas in the temporal context with time-series data.

The idea that patchiness decreases ($p$ increases) with increasing response time contradicts the concept that patchiness increases by the generation of fine-scale filaments formed by stirring a two-dimensional field (Abraham, 1998). The theory on two-dimensional stirring neglects the effect of upwelling, but this work considers the effect of continued upwelling on the surface fields. Although these results might be somewhat modified by including the effect of horizontal stirring, we believe that the surface signal of tracers that possess a steep concentration gradient across the thermocline is largely dominated by upwelling. Thus, these results quantify, to first order, the characteristics of the sea surface distribution of a tracer in response to ocean dynamics and nonconservative processes.

## 14.6 Conclusions

The analysis of satellite SST and Chl data over a range of length scales (2 to 256 km) shows that $V(L)$, the average variance contained in regions of area $L^2$, scales as $V(L) \sim L^p$. We propose the exponent $p$ as a measure of patchiness; smaller $p$ implies a larger percentage of the variance exists at small scales, and corresponds to greater patchiness. Satellite data shows that $p(\mathrm{Chl}) < p(\mathrm{SST})$, i.e., surface Chl is patchier than SST at meso- and submeso-scales. Likewise, other tracer distributions in the surface ocean differ in their spatial heterogeneity. The tracers considered have steep vertical concentration gradients, and surface concentration anomalies are introduced by upwelling. Differences in the spatial heterogeneity (and $p$) result from differences in the characteristic response times $\tau$ with which the tracers are modified by nonconservative processes in the upper ocean. Using a scaling argument and numerical model, we show that $p \sim \log \tau$. Tracers with relatively small $\tau$ have fine-scaled surface distributions, require higher resolution for modeling and sampling and have lower mean concentrations at the surface. For tracers differing in $\tau$, the grid spacing required scales as $\Delta \sim \exp(-1/\log \tau)$, and the ratio of the mean surface to deep concentrations scales as $c/c_\infty \sim 1/(1+\tau^{-1})$.

## Acknowledgments

We thank T. Moore for help with the analysis of satellite data. The SeaWiFS and MODIS data were obtained from the NASA Goddard DAAC. This work was sponsored by ONR (N00014-00-C-0079) and NASA (NAS5-96063 and NAG5-11258).

## References

Abraham, E., The generation of plankton patchiness by turbulent stirring, *Nature*, 391, 577–580, 1998.
Campbell, J.W. and Esaias, W.E., Spatial patterns in temperature and chlorophyll on Nantucket Schoals from airborne remote sensing data, May 7–9, 1981, *J. Mar. Res.,* 1985, 43, 139–161.
Denman, K.L. and Platt, T., Spectral analysis in ecology, *Annu. Rev. Ecol. Syst.,* 6, 189–210, 1975.

Deschamps, P.Y., Frouin, R., and Wald, L., Satellite determination of the mesoscale variability of the sea surface temperature, *J. Phys. Oceanogr.,* 11, 864–870, 1981.

Esaias, W.E. et al., 1998, An overview of MODIS capabilities for ocean science observations, *IEEE Trans. Geosci. Remote Sensing,* S6(4), 1250–1265, 1998.

Glover, D.M., Doney, S.C., Mariano, A.J., Evans, R.H., and McCue, S.J., Mesoscale variability in time series data: satellite-based estimates of the U.S. JGOFS Bermuda Atlantic Time-series Study (BATS) site, *J. Geophys. Res.*, 107(C8), 7-1 to 7-21, 2000.

Gower, J.F.R., Denman, K.L., and Holyer, R.J., Phytoplankton patchiness indicates the fluctuation spectrum of mesoscale oceanic structure, *Nature*, 288, 157–159, 1980.

Levitus, S., Climatological Atlas of the World Ocean, NOAA Professional Paper 13*,* 1982, 173 pp.

Levy, M., Klein, P., and Treguier, A.-M., Impacts of sub-mesoscale physics on production and subduction of phytoplankton in an oligotrophic regime, *J. Mar. Res.,* 59, 535–565, 2001.

Mahadevan, A. and Archer, D., Modeling the impact of fronts and mesoscale circulation on the nutrient supply and biogeochemistry of the upper ocean, *J. Geophs. Res*., 105, 1209–1225, 2000.

Mahadevan, A. and Campbell, J.W., Biogeochemical patchiness at the sea surface, *Geophys. Res. Lett.*, 29(19), 1926, doi: 10.1029/2001GLO14116, 2002.

McClain, E.P., Pichel, W.G., and Walton, C.C., Comparative performance of AVHRR-based multichannel sea surface temperatures, *Geophys. Res.*, 90(C), 11587–11601, 1985.

McClain, C.R., Cleave, M.L., Feldman, G.C., Gregg, W.W., Hooker, S.B., and Kurling, N., Science quality SeaWiFS data for global biosphere research, *Sea Technol.*, 10–16, Sept. 1998.

Pollard, R.T. and Regier, L.A., Vorticity and vertical circulation at an ocean front, *J. Phys. Oceanogr.,* 22, 609–625, 1992.

Semtner, A.J., Jr. and Chervin, R.M., Ocean general circulation from a global eddy-resolving model, *J. Geophs. Res.,* 97(C4), 5493–5550, 1992.

Voorhis, A.D. and Bruce, J.G., Small-scale surface stirring and frontogenesis in the subtropical convergence zone of the western North Atlantic, *J. Mar. Res.,* 40, S801–S821, 1982.

Yoder, J.A., McClain, C.R., Blanton, J.O., and Oey, L.-Y., Spatial scales in CZCS-chlorophyll imagery of the southeastern U.S. continental shelf, *Limnol. Oceanogr.*, 32, 929–941, 1987.

Yoder, J.A., Aiken, J., Swift, R.N., Hoge, F.E., and Stegmann, P.M., Spatial variability in the near-surface chlorophyll *a* fluorescence measured by the Airborne Oceanographic Lidar (AOL), *Deep Sea Res. II,* 40, 37–53, 1993.